PCCP

ROYAL SOCIETY OF CHEMISTRY

PAPER

View Article Online
View Journal | View Issue

Cite this: *Phys. Chem. Chem. Phys.*, 2024, **26**, 1225

Exploiting the photophysical features of DMAN template in ITQ-51 zeotype in the search for FRET energy transfer†

Ainhoa Oliden-Sánchez, [a] Rebeca Sola-Llano, [a] Joaquín Pérez-Pariente, [b] Luis Gómez-Hortigüela *[b] and Virginia Martínez-Martínez *[a]

Received 6th June 2023,
Accepted 6th December 2023

DOI: 10.1039/d3cp02625f

rsc.li/pccp

The combination between photoactive molecules and inorganic structures is of great interest for the development of advanced materials in the field of optics. Particularly, zeotypes with extra-large pore size are attractive because they allow the encapsulation of bulky dyes. The microporous aluminophoshate Mg-ITQ-51 (IFO-type structure) represents an ideal candidate because of the synergic combination of two crucial features: the IFO framework itself, which is composed of non-interconnected one-dimensional extra-large elliptical channels with a diameter up to 11 Å able to host bulky guest species, and the particular organic structure-directing agent used for the synthesis (1,8-bis(dimethylamino)naphthalene, DMAN), which efficiently fills the IFO pores, and is itself a photoactive molecule with interesting fluorescence properties in the blue range of the visible spectrum, thus providing a densely-incorporated donor species for FRET processes. Besides, occlusion of DMAN dye in the framework triggers a notable improvement of its fluorescence properties by confinement effect. To extend the action of the material and to mimic processes such as photosynthesis in which FRET is essential, two robust laser dyes with bulky size, rhodamine 123 and Nile Blue, have been encapsulated for the first time in a zeolitic framework, together with DMAN, in a straightforward one-pot synthesis. Thus, photoactive systems with emission in the entire visible range have been achieved due to a partial FRET between organic chromophores protected in a rigid aluminophosphate matrix.

1. Introduction

The design and production of new functional materials that respond to the technological requirements of today's world represents one of the greatest challenges in our current society. In the search for sophisticated technological applications, scientific research pursues the development of hybrid complex active materials that offer advanced properties notably overcoming those of traditional materials. In this context, research on hybrid materials containing photoactive units is an expanding field, providing interesting systems in the fields of optics, electronics, energy, environment, and many others.[1–5] When designing active systems with fluorescent organic dyes, one of the prerequisites is that the material must be optically dense for optical applications. However, many of these photoactive molecules have a relatively high tendency to self-associate under the necessary high concentrations (in aqueous solution or solid-state), which leads to a negative impact on the overall luminescent performance. Indeed, aggregates and monomers compete when absorbing the incident light, and the former ones are generally characterized as non-fluorescent, or much less fluorescent than monomers (except for very specific examples which follow aggregation induced emission, AEI, phenomena),[6–8] drastically decreasing the fluorescence capacity of the system. For this reason, self-aggregating photoactive molecules are usually occluded within molecular-sized confined spaces of microporous materials in order to prevent such self-aggregation and, at the same time, a potential photodegradation of the dye.[9–18] Furthermore, the photophysical properties of the enclosed fluorophores are usually enhanced by restricting molecular motions due to confinement effects for host–guest systems with proper size-match.[19–23] In this context, zeolitic materials with micropores of molecular size have been found as ideal host matrices for the encapsulation of photoactive molecules, and those built up by Mg-containing aluminophosphate networks are particularly interesting.[6,19,20,24,25]

In the background of artificial photosynthetic systems, one of the most interesting photophysical processes is the so-called

[a] *Departamento de Química Física, Universidad del País Vasco (UPV/EHU), Apartado 644, 4808 Bilbao, Spain. E-mail: ainhoa.oliden@ehu.eus, rebeca.sola@ehu.eus, virginia.martinez@ehu.eus*
[b] *Instituto de Catálisis y Petroleoquímica, CSIC, c/Marie Curie 2, 28049 Cantoblanco, Madrid, Spain. E-mail: lhortiguela@icp.csic.es, jperez@icp.csic.es*

† Electronic supplementary information (ESI) available: Specific gel molar compositions for hybrid systems; XRD patterns, ^{13}C CP MAS NMR, and TGA and CHN elemental analysis of Mg-ITQ-51 samples; photophysical study of DMAN in solution. See DOI: https://doi.org/10.1039/d3cp02625f

Förster resonance energy transfer (FRET), which is achieved by the simultaneous incorporation of organic species with compatible fluorescence properties.[25–28] FRET mechanisms consist in harvesting light through absorption of a donor molecule to subsequently transfer the energy to another acceptor component.[29–34] The efficiency of this process between chromophores is governed by the distance between chromophores and their relative orientations, as well as by the exact donor:-acceptor ratio.[35]

Indeed, the encapsulation of dyes into zeolitic structures allows the precise control of such parameters, otherwise unfeasible when the dyes are free in solution, with the aim of developing artificial antenna systems to be used in a wide range of applications, *e.g.* photonic antennas, tuneable dye-lasers, light modulators, and so on.[26,36–38]

Traditionally, the size of the guest photoactive molecules to be confined within zeolitic structures has been severely restricted due to the limited pore size of the host zeolite frameworks used, usually with pores smaller than 7 Å in diameter. However, many interesting dyes display sizes out of such limit, which notably limited the availability of zeolite/dye host/guest photoactive systems. Nonetheless, the development of new concepts in the synthesis of zeolites, in particular, the self-assembling templating (SAT) process, where bulky self-assembled aggregates of organic species are used as structure-directing agents (SDA) for the crystallization of zeolites, have enabled the discovery of extra-large pore new zeolite frameworks.[39–46] Among them, the ITQ-51 zeotype (IFO framework type), discovered in 2013, displays a particularly interesting structure for the encapsulation of bulky dyes, consisting of a one-dimensional 16-ring channel aluminophosphate framework with a pore opening of 11.3 Å × 8.4 Å (Fig. 1a).[47] This zeolite material was synthesized by using 1,8-bis(dimethylamino)naphthalene (DMAN) as structure-directing agent (SDA), an aromatic diamine with a very strong basicity ($pK_a < 12.3$).[48,49] This SDA was proved to self-assemble and form dimers during the crystallization of this framework, which stabilize its extra-large pores (Fig. 1b).[50]

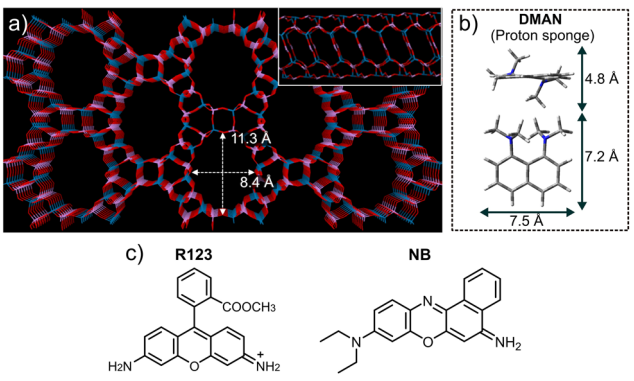

Fig. 1 (a) Illustrative representation of the IFO framework and view of the nanochannels (inset); the pore dimensions are indicated (calculated as interatomic distances subtracting the oxygen R_{vdW}). (b) Optimized geometry of DMAN (up and front view) with its molecular dimensions. (c) Molecular structures of rhodamine 123 (R123) and Nile Blue (NB) dyes.

Moreover, apart from the interesting geometric features of the IFO framework to provide a host matrix for the encapsulation of bulky photoactive guest species, this material entails another interesting feature for the development of FRET host–guest active systems associated to the SDA used for the synthesis (DMAN), which itself displays interesting fluorescent properties in the blue range of the visible spectrum. After crystallization, DMAN species fill the pores of the zeolitic framework, thus providing a densely-incorporated photoactive dye able to emit light. If combined with proper acceptor dyes, artificial antenna systems could be developed by using this zeolite material. Of the different IFO materials available,[51] Mg-containing IFO (Mg-ITQ-51) was selected since we know from our previous works that doping these aluminophosphate zeolitic networks with Mg notably enhances the incorporation of cationic dyes because of electrostatic interactions. On the other hand, cationic dyes with proper size to be incorporated in the framework were selected with the aid of molecular simulations; the IFO extra-large pores enabled the incorporation for the first time in zeolite materials of very large laser dyes such as rhodamine 123 (R123) and Nile Blue (NB), with a general molecular structure built up by three fused aromatic rings (Fig. 1c), and thus potentially susceptible to aggregation at high concentrations.

2. Experimental

2.1. Synthesis of Mg-ITQ-51 (IFO) materials

The syntheses of Mg-ITQ-51 materials were carried out using gels with molar composition: 0.95 Al_2O_3:1 P_2O_5:*x* MgO:1.2 DMAN:*y* H_2O:*z* dye; where *x* is 0.1 or 0.2, *y* is 40 or 100 and *z* is 0 for samples without dyes or 0.008 for samples with laser dye, respectively. DMAN (1,8-bis(dimethylamino)naphthalene, 99 wt%, proton sponge, Aldrich), Milli-Q H_2O and H_3PO_4 (85 wt%, Aldrich) were mixed and stirred for 2 hours. Then, a 20 wt% aqueous solution of magnesium chloride hexahydrate ($MgCl_2{\cdot}6H_2O$, Aldrich) was added and stirred for 20 min. Finally, the alumina (Al_2O_3, 75 wt%, Condea) was added to the gel and kept stirring for 30 min. The dyes, rhodamine 123 (R123; 3,6-diamino-9-(2-(methoxycarbonyl)phenyl)xanthylium chloride, Kodak, laser grade) and Nile Blue (NB; (5-aminobenzo[*a*]phenoxazin-9-ylidene)-diethylazanium, Exciton) were incorporated in this step into the gel, which was left under stirring for another hour. The gels were then transferred to autoclaves and heated in the oven at 150 °C under static conditions for 1 to 5 days. The specific gel molar compositions of the prepared samples are shown in Table S1 in the ESI.†

2.2. Quantification of dye loadings into Mg-ITQ-51 (IFO) materials

Photometric method. The final SDA (DMAN) and dye loadings incorporated into the aluminophosphate powders were quantified spectrometrically after dissolving a certain amount (10 mg) of the sample powder in hydrochloric acid (5 M). However, in the case of the SDA, since it was not very soluble in water, 50 : 50 H_2O : EtOH solutions were prepared to help the solubility of the

organic molecule in the media. The absorption spectra of the samples were compared with the absorptions of the previously prepared standard solutions (with known concentrations), making a calibration curve at analogous conditions. The absorption spectra were recorded with a UV-Vis spectrophotometer (Cary 7000), described below. Dye content values are given throughout this work as mmol of dye per 100 g sample powder and in percentage with respect to the initial amount added in the synthesis gel.

2.3. Structural characterization

X-Ray powder diffraction (PXRD) was used to identify the crystalline structures of the solids. The diffraction patterns were collected by using a Philips X'pert PRO automatic diffractometer with Cu-K radiation (λ = 1.5418 Å) and a PIXcel solid-state detector. The size and morphology of the samples were characterized by SEM in a JEOL JSM-6400 (tungsten filament) and a JEOL JSM-7000F (Schottky Field Emission Gun) operating at 20 kV and 10–11 A. These measurements were carried out at the University of the Basque Country UPV-EHU, SGIker facilities. Thermogravimetric analyses (TGA) were registered using a PerkinElmer TGA7 instrument (heating rate = 20 °C min^{-1}) under air flow. Solid state MAS-NMR spectra of the solid samples were recorded with a Bruker AV 400 WB spectrometer, using a BL7 probe. ^{1}H to ^{13}C cross-polarization spectra were recorded using $\pi/2$ rad pulses of 2.75 μs for ^{1}H, a contact time of 3 ms and a recycle delay of 4 s. The spectra were recorded while spinning the samples at *ca.* 11.2 kHz.

2.4. Photophysical characterization

Absorption spectra were recorded in a double beam Agilent Cary 7000 universal measurement spectrophotometer (UMS) with a Hamamatsu R928 photomultiplier as a detector, in transmittance for solutions (organic species, standards and dye-loading quantification), after baseline correction, and with an integrating sphere for bulk powder (Internal DRA 900). The absorbance like spectra of the powder samples was obtained after applying Kubelka–Munk function. Steady-state fluorescence measurements were carried out in an Edinburgh Instruments Spectrofluorimeter (FLSP920 model), with a photomultichannel tube, PMT (Hamamatsu R2658P) as a detector. Fluorescence quantum yields were determined *via* absolute method, through an integrating sphere in the same spectrofluorimeter. Laser flash photolysis (LP980, Edinburgh Instruments) was used to record emission spectra at different delay times after the laser pulse. The spectra were collected with an ICCD detector (Andor iStar). Samples were excited by a computer-controlled Nd:YAG laser coupled to OPO system from LOTIS TII (laser model LS-2134UT-UV3; OPO model LT-2215-PC working at 1 Hz). Fluorescence microscopy images were recorded with an optical upright wide field microscope with *epi* configuration (Olympus BX51) equipped with a color CCD camera (DP72) using: D350/50x band pass for UV excitation and 380DCLP dichroic and E400LPv2 cut-off for blue emission region, D470/70 for blue excitation and 495DCLP dichroic and E515LPv2 cut-off for green emission and HQ530/30m for green excitation and Q660LP dichroic and E580lp cut-off for the red emission region.

2.5. Computational details

Calculations on the location of dyes embedded within the IFO framework structure were based on a combination of molecular mechanics and DFT+D methods, as implemented in Forcite and CASTEP modules, in Materials Studio 2022 software. Molecular mechanics calculations were based on the cvff forcefield.[52] Plane waves DFT-D theoretical calculations have been performed with the CASTEP module in Material Studio[53] using PBE[54] as functional; the Grimme dispersion term[55] was used to account for dispersion interactions. Previous crystal-structure solution based on XRD results of ITQ-51[50] showed that the main 16-ring channels are filled by organic DMAN cations, and not by water molecules, and hence we have computationally studied models with IFO extra-large channels occupied by DMAN. The most stable location of DMAN cations was obtained by cvff simulated annealing calculations, followed by DFT+D geometry optimization (using 1 × 4 × 1 IFO supercells). The occlusion of R123 and NB dyes was obtained after Monte–Carlo simulations, followed by cvff simulated annealing and DFT+D geometry optimization. Energy results are given in kcal mol^{-1} of dye.

3. Results and discussion

3.1. Synthesis of Mg-ITQ-51 and photophysics of occluded DMAN

The Mg-doped IFO zeotype was synthesized following the original recipe,[47,51] from gels with molar composition 0.95 Al_2O_3: 1.00 P_2O_5:0.1 MgO:1.2 DMAN:40 H_2O, using DMAN as organic SDA and the divalent transition metal Mg^{2+} ion as heteroatom to generate negative charges in the framework that will be balanced by protonated DMAN species. The high basicity of DMAN (pK_a = 12.3) ensures its protonation in the synthesis medium (pH of the prepared gels is around 8), thus allowing the necessary organic–inorganic interactions during the nucleation–crystallization processes. The Mg-containing ITQ-51 materials were prepared by hydrothermal method at 150 °C under static conditions. In the original recipe, the IFO structure was obtained after heating for 5 days;[51] in the present study, different heating times were applied (1–5 days) with the aim of reducing the thermal treatment time and hence minimizing the potential dye degradation. Crystallization of pure Mg-ITQ-51 was confirmed by PXRD (Fig. S1 in the ESI†).[56] Interestingly, no apparent differences were observed among the different heating times, evidencing the successful crystallization of this phase even after 1 day of heating. Scanning electron microscopy images (Fig. 2a) show ITQ-51 crystalline particles, with no visible amorphous phases or crystals with different morphologies; the Mg-ITQ-51 samples show intergrown plate-like crystalline particles with sizes ranging from 5 to 10 μm.

As commonly found in the synthesis of zeolite materials through organic SDAs, a high incorporation of DMAN within the IFO framework has been achieved for all samples, with around 17–18 wt% of DMAN occluded in the solid (as determined from thermogravimetric, CHN analyses and

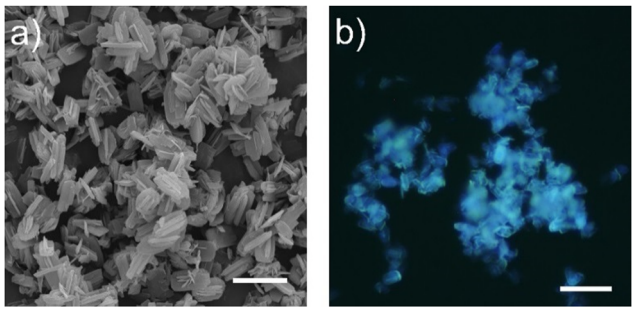

Fig. 2 (a) Mg-ITQ-51 particle images after 1 day of crystallization. SEM; scale = 10 μm. (b) Fluorescence image under UV excitation (D350/50x band-pass); scale = 20 μm.

photometric method, see ESI,† Fig. S2, S3 and Table S2), which corresponds to ~2 DMAN molecules per unit cell; this corresponds to 18% with respect to the initial amount added to the gel. Such high organic loadings may also explain the excellent structure direction driven by this aromatic molecule, resulting in a very pure phase and homogeneous crystallization. In addition, TGA shows that DMAN dye molecules are stable at least up to 200 °C (in air, Fig. S3, ESI†), showing a high thermal resistance of the confined dye.

DMAN itself is known to exhibit interesting photophysical properties in aqueous media (see Section S2 in the ESI† for more details on photophysics of this compound in solution at different concentrations and pHs, Fig. S5, S6 and Table S3). Thus, the first part of this photophysical study is dedicated to describing the photophysics of DMAN occluded into the IFO extra-large pores to be compared with the behavior of DMAN in aqueous solution. Mg-ITQ-51/DMAN particles analyzed by optical microscopy (Fig. 2b) show bright blue fluorescence under UV excitation light. The UV-Vis absorption spectrum of the bulk white powder of the Mg-ITQ-51/DMAN samples (prepared after 1 day of crystallization) shows the main band at 315 nm together with a very broad tail at higher wavelengths, from 450 to 700 nm (Fig. 3a).

Hence, the main absorption band of DMAN confined within the IFO cavities (Fig. 3), red-shifted with respect to the protonated DMAN-H^+ in solution (285 nm, Fig. S5a and Table S3 in the ESI†), is assigned mainly to the protonated DMAN, although a minor contribution of the neutral species cannot be excluded (characterized by an absorption band at 345 nm, see Section S2 in the ESI† and data in Table S3 and Fig. S5c). Upon excitation to this band (λ_{exc} = 315 nm, blue spectrum in Fig. 3b), a well-defined emission band appears centered at 412 nm (solid blue line), which is in agreement with previous studies of DMAN within IFO structure.[50] The excitation spectrum shows a band at 288 nm (Fig. 3b, dashed line), very similar to that registered for the DMAN-H^+ in aqueous solution (285 nm, Table S3 and Fig. S5a, ESI†) ensuring that protonated DMAN species is accountable for the fluorescence of the system. Note also here that although the monomer is present with a very small contribution with respect of its dimer, it is the main responsible for the emission due to the characteristic low fluorescence efficiency of dimers. Interestingly, this fluorescence efficiency for the trapped monomer DMAN-H^+ is much higher compared to that found in aqueous solution (24% *vs.* 1%, respectively), explaining the intense blue emission observed by optical microscopy in the Mg-ITQ-51 particles (Fig. 2b). This notable improvement of the fluorescent quantum yield can be attributed to the confinement effect provided by the IFO cavities, probably associated to the restricted motion of dimethylamino groups, reducing internal conversion processes.

The red shifted tail in the absorption spectra at 450–650 nm (Fig. 3a) is likely assigned to DMAN complexes, which are expected in the crystalline environment of the IFO structure; indeed, self-assembled DMAN aggregates filling the IFO pores have been found by Rietveld and molecular simulation studies.[50] The recorded emission spectra upon excitation to this band (λ_{exc} = 460 nm and λ_{exc} = 550 nm, Fig. 3c) confirm the formation of two weakly emissive complexes: one centered at around 540 nm and another at longer wavelengths at around 650 nm (similar to the emission band found in solution, Fig. S5 in ESI†). These two emission bands (see ESI†) could be assigned to excimers and complexes with inter charge transfer (interCT) nature, respectively, from protonated DMAN species, coexisting within IFO pores. Note here that the emission efficiency of those complexes is much lower in comparison with the isolated DMAN molecules. The excitation spectrum registered at long emission wavelengths (λ_{em} = 660 nm) shows, together with the main UV band, a red shifted characteristic band (Fig. 3c) similar to that obtained in the absorption spectra (Fig. 3a), confirming the aforementioned assignation. Indeed, this band appears slightly red shifted and with a more-defined shape than that observed in the absorption spectrum (Fig. 3a), indicating a higher contribution of these complexes in the excited state. This is a typical feature of interCT complexes but not of excimers, as the latter only exist in the excited electronic state because they dissociate after photon emission.

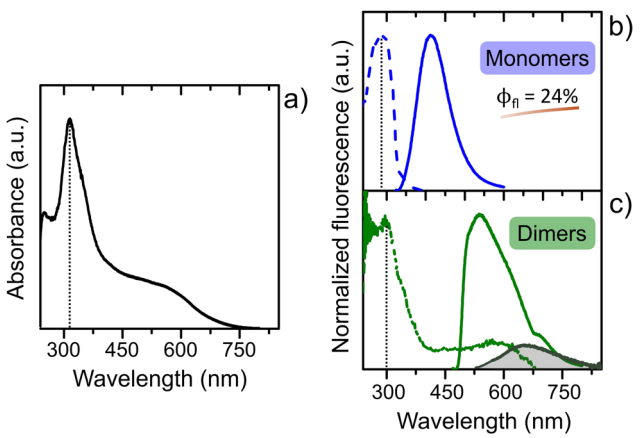

Fig. 3 Photophysical characterization of Mg-ITQ-51/DMAN material in bulk powder: (a) absorption (black), (b) height normalized excitation (dashed blue, at λ_{em} = 450 nm) and emission spectra (solid line at λ_{exc} = 315 nm) for the DMAN monomer and (c) height normalized excitation (dashed green, at λ_{em} = 650 nm) and emission spectra (solid green and grey at λ_{exc} = 460 and 550 nm, respectively).

Therefore, the incorporation of the structure-directing agent DMAN takes place both in its monomeric (although in a minor extension) and associate states (which should represent the main species present according to the previous Rietveld study[50] and to our experimental packing of 2.0 DMAN/u.c., as determined from TGA and CHN analyses and photometric method), resulting in feasible self-interactions of the DMAN molecules in the synthesis gel and the final Mg-ITQ-51 solid prepared.[50] On the other hand, a highly fluorescent material has been obtained as a consequence of the enhanced photophysical properties of the constrained monomer units.

Surprisingly, the fluorescent properties of the DMAN molecules are strongly affected by the aging time of the hybrid system. Several months after the original synthesis of the material, a sharp decrease in the fluorescent emission was detected in all samples. Optical microscopy images (Fig. 4) show this abrupt change in intensity and color hue over time, being possible to discern particles with a weak green color from others which are practically not fluorescent. This strange phenomenon in the material was not expected in such stable materials as zeotypes; indeed, long-term stability of the IFO framework was evidenced by XRD (see ESI,† Fig. S1-bottom). Hence, in an attempt to understand the change in the system's behavior, the photophysics of the aged system was characterized. All these data are included in Table 1. The most notable change was observed in terms of the fluorescent quantum yield of the DMAN, registering a very sharp decrease from 24% to 5% (Fig. 4c). In addition, the emission spectra recorded for the aggregates (Fig. 4d) showed a narrower and bathochromically shifted band (at around 600 nm) with respect to the previous one. One of the hypotheses for this photophysical change is a geometrical redistribution of the DMAN species within the ITQ-51 structure with time.

Table 1 Photophysical parameters: absorption (λ_{abs}) and fluorescence maximum (λ_{fl}) wavelengths, of DMAN monomers and dimers within the MgIFO structure over time

Sample	DMAN	λ_{abs} (nm)	λ_{fl} (nm)	φ_{fl}
MgIFO	Monomers	316.0	412.0	0.24
	Dimers	450–650[a]	536.0	<0.01
MgIFO (aged)	Monomers	316.0	412.0	0.05
	Dimers	450–650[a]	603.0	<0.01

Fluorescence quantum yields were recorded upon excitation at 315 nm for DMAN monomers and 460 nm for the dimers. [a] Tail in the absorption spectra.

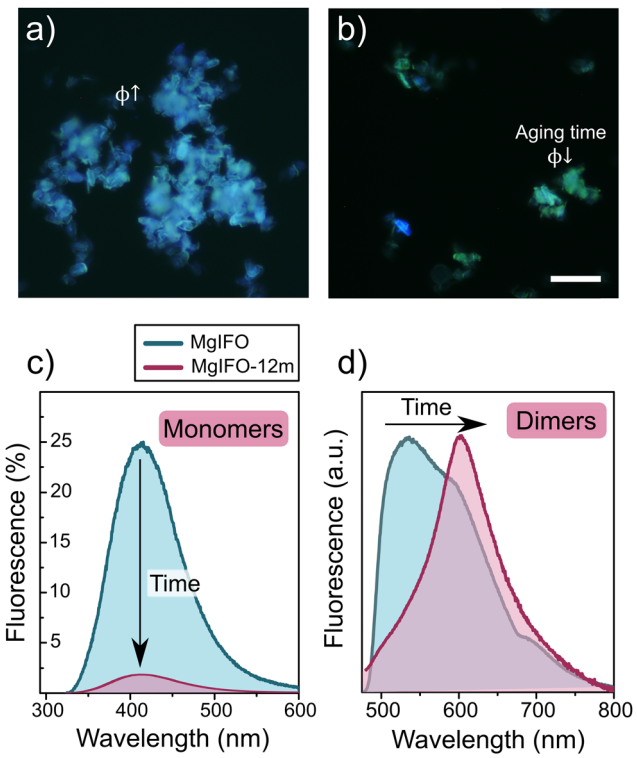

Fig. 4 Fluorescence images of Mg-ITQ-51 particles under UV excitation (D350/50x band-pass) (a) right after synthesis and (b) a few months later. Scale = 20 μm. (c) Photophysical changes in the Mg-ITQ-51 material after 12 months, from blue to red-colored spectrum: fluorescence spectrum of DMAN monomers (λ_{exc} = 315 nm), and (d) height normalized fluorescence spectra of DMAN dimers (λ_{exc} = 460 nm).

To elucidate the formation of aggregates of DMAN cations within the IFO structure, a computational study based on a combination of force-field-based and periodic plane-wave DFT+D methods was performed. After an exhaustive search by simulated annealing calculations, two types of configurations for the DMAN cations filling the IFO pores were identified; the DFT+D optimized geometries of both DMAN configurations are shown in Fig. 5. Energy results reveal a similar stability for DMAN cations in both configurations; it should be noted that Mg has not been implicitly included in the calculations, and hence specific $DMAN^{+}\cdots Mg(^{-})$ interactions (negative charge of Mg arising from the $Mg^{2+} \leftrightarrow Al^{3+}$ replacement) in both types of configurations are not taken into account. Fig. 5a depicted a possible configuration in which the naphthalene unit of one of the monomers locates in front of the DMA groups of the second monomer, favoring a charge transfer process between both moieties (being the DMA group the electron-donor and the aromatic naphthalene the electron acceptor); this configuration coincides with that reported previously after the Rietveld and molecular simulation study.[50] A second plausive configuration involves a rotation of the DMAN species perpendicular to the channel axis, locating the naphthalene groups in a face-to-face configuration and enabling π–π type interactions between the aromatic rings, being the typical conformation of exciplexes (Fig. 5b).

The two arrangements seek to maximize interaction between the aromatic rings of DMAN species and the packing efficiency within the IFO framework, and the small energetic difference between the two predicts a potential formation of both types of configurations, possibly influenced by kinetic factors during crystallization as well as for the specific $DMAN^{+}\cdots Mg(-)$ interactions. These two types of DMAN arrangements can explain the photophysical observations about the formation of two types of self-assembled aggregates.

According to the computational model, both configurations are plausive and likely can coexist within IFO channels.

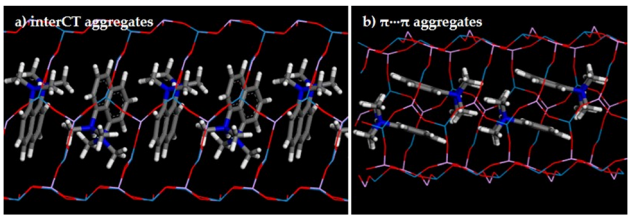

Fig. 5 Two possible stable configurations for DMAN aggregates within the IFO structure: (a) with inter charge transfer character, with the DMA and naphthalene groups, face to face, and (b) with π···π type interactions, with the aromatic naphthalene groups face to face.

Note here that the aging time could favor the redistribution of aggregates to those with interCT character, which would explain the new emission band at 603 nm (Fig. 4d and Table 1), compared to dimers with π–π interactions between aromatic rings[40] (maximum at 536 nm, Table 1). Moreover, the formation in a higher extent of less fluorescent dimers from monomer association would also explain the general drop in the fluorescent quantum yield in the system, probably associated also to a rearrangement of the strongly fluorescent monomers into less-fluorescent CT dimers. Thus, potential rearrangement of the host–guest systems becomes a new variable that should be taken into account when studying these systems.

3.2. Co-encapsulation with laser dyes for energy transfer (FRET)

In light of the above results, a hybrid zeolitic material with blue emission as a consequence of the organic SDA is available. In order to increase the fluorescent response range, energy transfer processes between photoactive units of different entities were then pursued by the encapsulation of other fluorescent dyes into the unidirectional channels of the framework together with DMAN. In this sense, considering that the DMAN-IFO zeotype emits mainly in the blue region, two commercially available and widely known laser dyes, rhodamine 123 (R123, λ_{abs} = 498 nm and λ_{fl} = 525 nm in H_2O) and Nile Blue (NB, λ_{abs} = 635 nm and λ_{fl} = 674 nm in H_2O), with green and red emission properties, respectively, have been selected as suitable FRET pairs with DMAN and thus allowing to tune the final emission color of the system. Docking Monte-Carlo simulations showed that these two dyes, despite their large size, can be accommodated within the IFO extra-large pores (Fig. 6); energy results showed a better fit for NB than for R123, as indicated by its notably larger interaction energy (−62.5 kcal mol^{-1} for R123 and −77.0 kcal mol^{-1} for NB, calculated after simulated annealing with the cvff forcefield); indeed, host–guest fit of the largest R123 dye seems even too tight.

The dyes were added to synthesis gels with the same composition previously described for Mg-ITQ-51:0.95 Al_2O_3:1.00 P_2O_5:0.1 MgO:1.2 DMAN:40 H2O:0.008 dye (R123 and/or NB; see Table S1 in ESI† for exact molar composition of the gels). Note here that the total amount of dye added was kept low (x = 0.008) with respect to DMAN, in an attempt to not disrupt the crystallization of the IFO phase. The gels were heated at 150 °C for 24 h, the optimum time considered in the previous section for IFO crystallization.

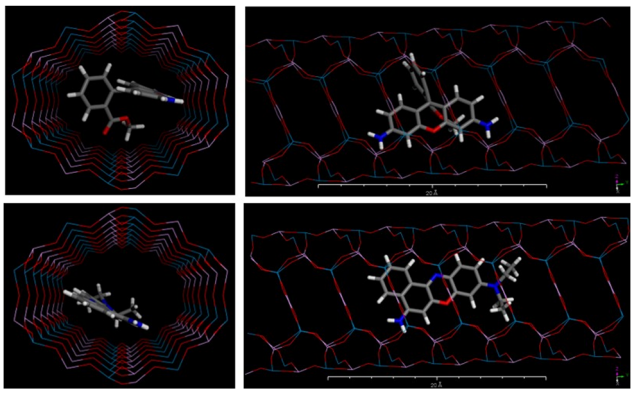

Fig. 6 Two views of the DFT-optimized structure of R123 (top) and NB (bottom) confined within the IFO nanochannels.

The PXRD patterns show that the addition of the dyes to the synthesis gels does not alter the formation of Mg-ITQ-51, obtaining a pure IFO structure (Fig. S1 in ESI†). In the material prepared in the presence of R123 (R123/MgIFO), the incorporation of the dye was found to be low (0.03 mmol of dye per 100 g of sample powder), but its presence is clearly evidenced from the absorption spectra by its characteristic band at 514 nm together with the main absorption peak of DMAN at 315 nm (data shown in Table 2 and Fig. 7b). Regardless of the excited species, either DMAN (λ_{exc} = 315 nm) or directly R123 (λ_{exc} = 480 nm), the rhodamine emission is observed at 538.0-540.0 nm (Table 2), which is responsible for the green emission of the hybrid system (Fig. 7a). R123/MgIFO sample shows an intense green fluorescence in comparison with the faint yellowish emission of MgIFO without dye using the same dichroic and emission filters (Fig. S4a in the ESI†). Hence, a FRET process is taking place from DMAN acting as donor to R123 acting as acceptor. The excitation spectrum (Fig. 7c) provides further evidence of this transfer showing DMAN monomers contribution to the R123 emission. However, the energy transfer process is not complete since upon direct excitation of DMAN, emission bands from both species (DMAN and R123) are detected (Fig. 7b).

In the case of the material containing NB, quantification indicates that the laser-dye incorporation has been slightly higher (0.045 mmol dye/100 g sample) than that of R123 (0.03 mmol/100 g sample), which is explained by the better host–guest fit of NB with respect to R123, as suggested by our

Table 2 Photophysical parameters: absorption (λ_{abs}) and fluorescence maximum (λ_{fl}) wavelengths of the dye-doped MgIFO samples

Sample	Dye	λ_{abs} (nm)	λ_{fl} (nm)
R123/MgIFO	DMAN	315.0	417.0
	R123	514.0	538.0
NB/MgIFO	DMAN	316.0	418.0
	NB	595.0[a]	628.5

[a] Value obtained from the excitation spectrum.

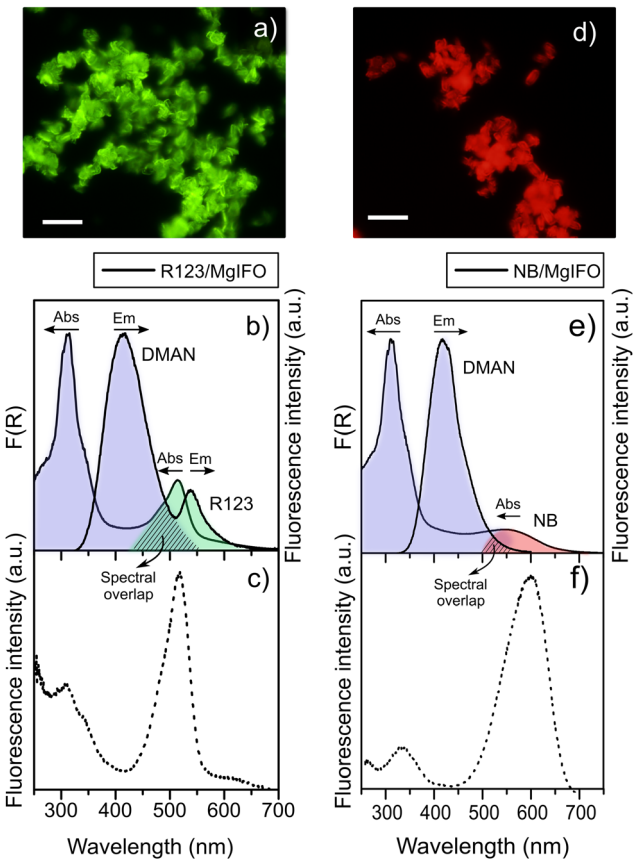

Fig. 7 Fluorescence images of R123/MgIFO (a) and NB/MgIFO (d) crystals; height normalized absorption and emission spectra (recorded upon 315 nm excitation) of the bulk powders R123/MgIFO (b) and NB/MgIFO (e) excitation spectra (recorded at 700 nm emission) for R123/MgIFO (c) and NB/MgIFO (f).

molecular simulations study (in terms of a more negative interaction energy). Such laser-dye incorporations are much lower than that of DMAN dye used as SDA, leading to D:A ratios between 35–75 : 1. However, as it has been proved in previous works, FRET in 1D ordered systems generally requires relative high ratios between D : A units.[24] Thus, particles of this NB/MgIFO material show a higher red fluorescence with respect to MgIFO without NB recorded at the same conditions, presumably evidencing the presence of the oxazine-type chromophore (Fig. 7d *vs.* Fig. S4b, ESI†). The absorption spectrum of the bulk powder shows the characteristic UV peak of DMAN species together with a broad band extended at higher wavelengths, (Fig. 7e). However, the confirmation of the incorporation of the NB dye is not trivial since it overlaps with the contribution of the DMAN complexes (Table 1 and Fig. 3a). However, from the excitation spectrum (Fig. 7f) the incorporation of NB within the MgIFO zeotype is confirmed by the appearance of a well-defined band at around 595 nm. However, the fluorescence band of NB under DMAN excitation is not detected indicating that in this case, the energy transfer is much less efficient than in the previous system with R123 (sample R123/MgIFO) as a consequence of the lower overlap between the emission spectra of the DMAN donor and the absorption band of the NB acceptor (with absorption above 600 nm), which is considered one of the key factors for FRET process. Note here that the estimation of FRET efficiency by the decrease of the fluorescence intensity of DMAN donor molecules in the presence of R123 or NB is not trivial and it can yield to misleading values since within the pores there are diverse DMAN species (monomers and aggregates) with different emission properties, which are also, time dependent.

In summary, although optimization is required in terms of dye occlusion loadings, this work presents systems in which a partial FRET process takes place from the organic template DMAN to two different laser co-encapsulated dyes in a unique step into the extra-large pores of the IFO structure, enabling the production of hybrid photoactive materials with broadened emission throughout different regions of the visible spectrum. Moreover, to a certain extent, it is possible to collect the emission from the laser dyes without exciting them directly, thereby prolonging the (photo)stability of the system.

Conclusions

The extra-large pore Mg-containing aluminophosphate zeotype Mg-ITQ-51, with IFO structure, has been shown to display blue fluorescent properties without the need to incorporate additional dyes into the synthesis gel due to the intrinsic emissive characteristics of the organic cation (1,8-dimethylaminonaphtalene) used as structure-directing agent for the crystallization of the framework. Indeed, confinement of these DMAN cations within the IFO framework involves a remarkable increase of the fluorescent quantum yield. Moreover, the self-assembling behavior of the protonated aromatic cation determines the resultant photophysical properties of the extra-large pore zeolite. It has been demonstrated that this material shows photophysical changes over time, due to the fact that the organic structure-directing agent (DMAN) employed for its crystallization exhibits a redistribution within the unidirectional IFO channels. Nevertheless, a thorough analysis was out of the scope of the current study and will be considered for the future.

Based on this starting fluorescent zeotype, the fluorescence range of the material has been broadened by combining dyes of large size, able to be hosted in the extra-large pores of this framework, with emission properties in the green and red regions of the visible spectrum, inducing FRET processes between the template DMAN and the encapsulated dyes. In this way, R123-MgIFO system has extended the emission from the blue to the green range, collecting it emission by indirect excitation.

Author contributions

Investigation A. O.-S.; computational investigation L. G.-H.; conceptualization A. O.-S., L. G.-H., V. M. M.; supervision R. S.-L., V. M.-M., L. G.-H. and J. P.-P.; project administration V. M.-M.; writing – original draft preparation and editing

R. S.-L. and A. O.-S.; revision manuscript V. M.-M, L. G.-H. and J. P.-P. All authors have read and agreed to the published version of the manuscript.

Conflicts of interest

The authors have no conflicts to disclose.

Acknowledgements

This research was supported by MCIN/AEI/10.13039/501100011033 (projects PID2020-114347RB-C32 and PID2019-107968RB-I00), and Gobierno Vasco – Eusko Jaurlaritza (project IT1639-22). Centro Técnico de Informática-CSIC is acknowledged for running the calculations and BIOVIA for providing the computational software. The authors thank for technical and human support provided by SGIker (UPV/EHU/ ERDF, EU).

Notes and references

1 L. Nicole, C. Laberty-Robert, L. Rozes and C. Sanchez, Hybrid materials science: a promised land for the integrative design of multifunctional materials, *Nanoscale*, 2014, **6**, 6267–6292.
2 G. Kickelbick, *Hybrid Materials: Synthesis, Characterization, and Applications*, 2007.
3 S. Parola, B. Julián-López, L. D. Carlos and C. Sanchez, Optical Properties of Hybrid Organic-Inorganic Materials and their Applications, *Adv. Funct. Mater.*, 2016, **26**, 6506–6544.
4 L. G. Rivero, J. Bañuelos, K. Bizkarra, U. Izquierdo, V. L. Barrio, J. F. Cambra and I. L. Arbeloa, in *Zeolites and Their Applications*, ed. M. N. Rashed and P. N. Palanisamy, InTech, 2018, ch. 2, DOI: 10.5772/intechopen.73135.
5 J. Bujdák, T. S. Baranyaiová, P. Boháč and R. Mészáros, Adsorption of Dye Molecules and Its Potential for the Development of Photoactive Hybrid Materials Based on Layered Silicates, *J. Phys. Chem. B*, 2023, **127**, 1063–1073.
6 R. Sola-Llano, Y. Fujita, L. Gómez-Hortigüela, A. Alfayate, H. Uji-I, E. Fron, S. Toyouchi, J. Pérez-Pariente, I. López-Arbeloa and V. Martínez-Martínez, One-Directional Antenna Systems: Energy Transfer from Monomers to J-Aggregates within 1D Nanoporous Aluminophosphates, *ACS Photonics*, 2018, **5**, 151–157.
7 F. Würthner, Aggregation-induced emission (AIE): a historical perspective, *Angew. Chem., Int. Ed.*, 2020, **59**, 14192–14196.
8 H. Wang and G. Liu, Advances in luminescent materials with aggregation-induced emission (AIE) properties for biomedical applications, *J. Mater. Chem. B*, 2018, **6**, 4029–4042.
9 M. Handke, T. Adachi, C. Hu and M. D. Ward, Encapsulation of isolated luminophores within supramolecular cages, *Angew. Chem., Int. Ed.*, 2017, **56**, 14003–14006.
10 V. Martínez, R. García Salas, L. Gómez-Hortigüela Sainz, J. Pérez Pariente and Í. López-Arbeloa, Modulating Dye Aggregation by Incorporation into 1D-MgAPO Nanochannels, *Chem. – Eur. J.*, 2013, **19**, 9859–9865.
11 M. Lal, L. Levy, K. S. Kim, G. S. He, X. Wang, Y. H. Min, S. Pakatchi and P. N. Prasad, Silica nanobubbles containing an organic dye in a multilayered organic/inorganic heterostructure with enhanced luminescence, *Chem. Mater.*, 2000, **12**, 2632–2639.
12 P. Innocenzi, E. Miorin, G. Brusatin, A. Abbotto, L. Beverina, G. A. Pagani, M. Casalboni, F. Sarcinelli and R. Pizzoferrato, Incorporation of Zwitterionic Push– Pull Chromophores into Hybrid Organic– Inorganic Matrixes, *Chem. Mater.*, 2002, **14**, 3758–3766.
13 K. Yagi, S. Shibata, T. Yano, A. Yasumori, M. Yamane and B. Dunn, Photostability of the laser dye DCM in various inorganic-organic host matrices, *J. Sol-Gel Sci. Technol.*, 1995, **4**, 67–73.
14 W. Chen, Y. Zhuang, L. Wang, Y. Lv, J. Liu, T.-L. Zhou and R.-J. Xie, Color-tunable and high-efficiency dye-encapsulated metal–organic framework composites used for smart white-light-emitting diodes, *ACS Appl. Mater. Interfaces*, 2018, **10**, 18910–18917.
15 K. Senthilkumar, P. Paul, C. Selvaraju and P. Natarajan, Preparation, characterization, and photophysical study of thiazine dyes within the nanotubes and nanocavities of silicate host: influence of titanium dioxide nanoparticle on the protonation and aggregation of dyes, *J. Phys. Chem. C*, 2010, **114**, 7085–7094.
16 F. Biedermann, E. Elmalem, I. Ghosh, W. M. Nau and O. A. Scherman, Strongly fluorescent, switchable perylene bis (diimide) host–guest complexes with cucurbit [8] uril in water, *Angew. Chem.*, 2012, **124**, 7859–7863.
17 A. Ray, S. Das and N. Chattopadhyay, Aggregation of Nile red in water: Prevention through encapsulation in β-cyclodextrin, *ACS Omega*, 2019, **4**, 15–24.
18 N. Zhang, D. Zhang, J. Zhao and Z. Xia, Fabrication of a dual-emitting dye-encapsulated metal–organic framework as a stable fluorescent sensor for metal ion detection, *Dalton Trans.*, 2019, **48**, 6794–6799.
19 A. Oliden-Sánchez, R. Sola-Llano, I. López-Arbeloa and V. Martínez-Martínez, Enhancement of NIR emission by a tight confinement of a hemicyanine dye within zeolitic MgAPO-5 nanochannels, *Photochem. Photobiol. Sci.*, 2018, **17**, 917–922.
20 R. Sola-Llano, V. Martínez-Martínez, Y. Fujita, L. Gómez-Hortigüela, A. Alfayate, H. Uji-i, E. Fron, J. Pérez-Pariente and I. López-Arbeloa, Formation of a Nonlinear Optical Host–Guest Hybrid Material by Tight Confinement of LDS 722 into Aluminophosphate 1D Nanochannels, *Chem. – Eur. J.*, 2016, **22**, 15700–15711.
21 A. L. Koner and W. M. Nau, Cucurbituril Encapsulation of Fluorescent Dyes, *Supramol. Chem.*, 2007, **19**, 55–66.
22 E. Arunkumar, C. C. Forbes and B. D. Smith, Improving the properties of organic dyes by molecular encapsulation, *Eur. J. Org. Chem.*, 2005, 4051–4059.
23 M. Mitsui, K. Higashi, R. Takahashi, Y. Hirumi and K. Kobayashi, Enhanced photostability of an anthracene-based dye due to supramolecular encapsulation: a new type of photostable fluorophore for single-molecule study, *Photochem. Photobiol. Sci.*, 2014, **13**, 1130–1136.
24 V. Martínez-Martínez, R. García, L. Gómez-Hortigüela, R. Sola Llano, J. Pérez-Pariente and I. López-Arbeloa, Highly Luminescent and Optically Switchable Hybrid Material by One-Pot Encapsulation of Dyes into MgAPO-11 Unidirectional Nanopores, *ACS Photonics*, 2014, **1**, 205–211.

25 R. Sola-Llano, A. Oliden-Sánchez, A. Alfayate, L. Gómez-Hortigüela, J. Pérez-Pariente, T. Arbeloa, J. Hofkens, E. Fron and V. Martínez-Martínez, White light emission by simultaneous one pot encapsulation of dyes into one-dimensional channelled aluminophosphate, *Nanomaterials*, 2020, **10**, 1173.
26 G. Calzaferri, H. Li and D. Brühwiler, Dye-modified nanochannel materials for photoelectronic and optical devices, *Chem. – Eur. J.*, 2008, **14**, 7442–7449.
27 D.-D. Hu, J. Lin, Q. Zhang, J.-N. Lu, X.-Y. Wang, Y.-W. Wang, F. Bu, L.-F. Ding, L. Wang and T. Wu, Multi-step host–guest energy transfer between inorganic chalcogenide-based semiconductor zeolite material and organic dye molecules, *Chem. Mater.*, 2015, **27**, 4099–4104.
28 Y. Wang, J. Zheng, J. Wang, Y. Yang and X. Liu, Rapid microwave-assisted synthesis of highly luminescent nitrogen-doped carbon dots for white light-emitting diodes, *Opt. Mater.*, 2017, **73**, 319–329.
29 D. R. Whang and D. H. Apaydin, Artificial photosynthesis: Learning from nature, *ChemPhotoChem*, 2018, **2**, 148–160.
30 D. Gust, T. A. Moore and A. L. Moore, Mimicking photosynthetic solar energy transduction, *Acc. Chem. Res.*, 2001, **34**, 40–48.
31 M. E. El-Khouly, E. El-Mohsnawy and S. Fukuzumi, Solar energy conversion: From natural to artificial photosynthesis, *J. Photochem. Photobiol., C*, 2017, **31**, 36–83.
32 L. Chen, P. Shenai, F. Zheng, A. Somoza and Y. Zhao, Optimal energy transfer in light-harvesting systems, *Molecules*, 2015, **20**, 15224–15272.
33 M. Şener, J. Strümpfer, J. Hsin, D. Chandler, S. Scheuring, C. N. Hunter and K. Schulten, Förster energy transfer theory as reflected in the structures of photosynthetic light-harvesting systems, *Chem. Phys. Chem.*, 2011, **12**, 518–531.
34 K. E. Sapsford, L. Berti and I. L. Medintz, Materials for fluorescence resonance energy transfer analysis: beyond traditional donor-acceptor combinations, *Angew. Chem., Int. Ed.*, 2006, **45**, 4562–4589.
35 J. R. Lakowicz, *Principles of fluorescence spectroscopy*, Springer Science & Business Media, 2013.
36 Y. Huang, F. Qiu, R. Chen, D. Yan and X. Zhu, Fluorescence resonance energy transfer-based drug delivery systems for enhanced photodynamic therapy, *J. Mater. Chem. B*, 2020, **8**, 3772–3788.
37 M. Stanisavljevic, S. Krizkova, M. Vaculovicova, R. Kizek and V. Adam, Quantum dots-fluorescence resonance energy transfer-based nanosensors and their application, *Biosens. Bioelectron.*, 2015, **74**, 562–574.
38 V. Anand and R. Dhamodharan, White light emission from fluorene-EDOT and phenothiazine-hydroquinone based D-π-A conjugated systems in solution, gel and film forms, *New J. Chem.*, 2017, **41**, 9741–9751.
39 C. Paris and M. Moliner, *Insights into the Chemistry of Organic Structure-Directing Agents in the Synthesis of Zeolitic Materials*, Springer, 2018, pp. 139–177.
40 A. Corma, F. Rey, J. Rius, M. J. Sabater and S. Valencia, Supramolecular self-assembled molecules as organic directing agent for synthesis of zeolites, *Nature*, 2004, **431**, 287–290.
41 M. Moliner, Design of zeolites with specific architectures using self-assembled aromatic organic structure directing agents, *Top. Catal.*, 2015, **58**, 502–512.
42 F. Chen, Y. Xu and H. Du, An Extra-Large-Pore Zeolite with Intersecting 18-, 12-, and 10-Membered Ring Channels, *Angew. Chem., Int. Ed.*, 2014, **53**, 9592–9596.
43 Z. Gao, F. Chen, L. Xu, L. Sun, Y. Xu and H. Du, A Stable Extra-Large-Pore Zeolite with Intersecting 14-and 10-Membered-Ring Channels, *Chem. – Eur. J*, 2016, **22**, 14367–14372.
44 D.-R. Liu, Z.-H. Gao, W.-W. Zi, J. Zhang, H.-B. Du and F.-J. Chen, Facile synthesis of large-pore zeolite ITQ-26 by using an easily-available imidazolium as structure-directing agent, *Microporous Mesoporous Mater.*, 2019, **276**, 232–238.
45 R. Martínez-Franco, A. Cantín, A. Vidal-Moya, M. Moliner and A. Corma, Self-assembled aromatic molecules as efficient organic structure directing agents to synthesize the silicoaluminophosphate SAPO-42 with isolated Si species, *Chem. Mater.*, 2015, **27**, 2981–2989.
46 L. Gómez-Hortigüela, F. López-Arbeloa, F. Cora and J. Pérez-Pariente, Supramolecular chemistry in the structure direction of microporous materials from aromatic structure-directing agents, *J. Am. Chem. Soc.*, 2008, **130**, 13274–13284.
47 R. Martínez-Franco, M. Moliner, Y. Yun, J. Sun, W. Wan, X. Zou and A. Corma, Synthesis of an extra-large molecular sieve using proton sponges as organic structure-directing agents, *Proc. Natl. Acad. Sci. U. S. A.*, 2013, **110**, 3749–3754.
48 A. Szemik-Hojniak, W. Rettig and I. Deperasińska, The forbidden emission of protonated proton sponge, *Chem. Phys. Lett.*, 2001, **343**, 404–412.
49 A. Szemik-Hojniak, G. Balkowski, G. W. H. Wurpel, J. Herbich, J. H. Van Der Waals and W. J. Buma, Photophysics of 1,8-Bis(dimethylamino)naphthalene in Solution: Internal charge transfer with a twist, *J. Phys. Chem. A*, 2004, **108**, 10623–10631.
50 R. Martínez-Franco, J. Sun, G. Sastre, Y. Yun, X. Zou, M. Moliner and A. Corma, Supra-molecular assembly of aromatic proton sponges to direct the crystallization of extra-large-pore zeotypes, *Proc. R. Soc. A*, 2014, **470**, 20140107.
51 R. Martínez-franco, C. Paris, M. Moliner, A. Corma and M. Moliner, Synthesis of highly stable metal-containing extra-large- pore molecular sieves, *Philos. Trans. R. Soc. London*, 2015, **374**, 20150075.
52 L. B. McCusker, D. H. Olson and C. Baerlocher, *Atlas of Zeolite Framework Types*, 2007.
53 P. Dauber-Osguthorpe, V. A. Roberts, D. J. Osguthorpe, J. Wolff, M. Genest and A. T. Hagler, Structure and energetics of ligand binding to proteins: Escherichia coli dihydrofolate reductase-trimethoprim, a drug-receptor system, *Proteins: Struct., Funct., Bioinf.*, 1988, **4**, 31–47.
54 S. J. Clark, M. D. Segall, C. J. Pickard, P. J. Hasnip, M. I. J. Probert, K. Refson and M. C. Payne, First principles methods using CASTEP, *Z. Kristallogr. Mater.*, 2005, **220**, 567–570.
55 J. P. Perdew, K. Burke and M. Ernzerhof, Generalized gradient approximation made simple, *Phys. Rev. Lett.*, 1996, **77**, 3865.
56 S. Grimme, Accurate description of van der Waals complexes by density functional theory including empirical corrections, *J. Comput. Chem.*, 2004, **25**, 1463–1473.